

Physics Laboratory

Measurements of environmental radioactivity

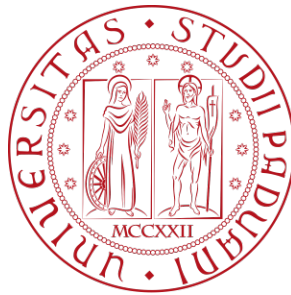
Group 23

Rasera Benedetta (2141189), Errico Antonio Romano (2157550), Magherini Federico (2152811)

benedetta.rasera@studenti.unipd.it
antonioromano.errico@studenti.unipd.it
federico.magherini@studenti.unipd.it

A.A. 2024/2025

Laboratory dates : 19,20 and 21/11/2024



Università degli Studi di Padova

Dipartimento di Fisica e Astronomia “Galileo Galilei”

Master’s Degree in Physics

Contents

| | | |
|----------|----------------------------------------------------|-----------|
| 1 | Introduction | 1 |
| 2 | Experimental Setup | 1 |
| 3 | Signal Processing and Trapezoidal Filtering | 1 |
| 4 | Detectors calibration | 1 |
| 4.1 | NaI(Tl) calibration | 2 |
| 4.2 | HPGe calibration | 3 |
| 5 | Samples analysis | 7 |
| 6 | Radon counting | 11 |
| 7 | Conclusions | 13 |

1. Introduction

The primary aim of this project is to fully characterize two detectors, NaI(Tl) and HPGe, in terms of energy calibration and efficiency using known radioactive sources. Following this, the detectors are employed to measure the environmental radioactivity of various organic and inorganic samples. Additionally, the project includes estimating the activity of radon ^{222}Rn through direct measurement using the activated-carbon canister method in a controlled environment within the Laboratory of Physics.

2. Experimental Setup

The experimental apparatus is designed to measure gamma radiation using two distinct types of detectors: a NaI(Tl) scintillation detector and a high-purity germanium (HPGe) detector, both housed in a shielded well. The NaI(Tl) detector is a cylinder measuring $7.5\text{ cm} \times 7.5\text{ cm}$, which is coupled to a photomultiplier tube (PMT). The PMT operates at a fixed voltage of $+700\text{ V}$ and is connected to a voltage divider that powers the dynodes and anode. The anode provides a direct output for time measurements, while the preamplifier processes the signal for energy measurements.

The HPGe detector, a semiconductor detector, is maintained at cryogenic temperatures using liquid nitrogen. It operates at -1800 V and is equipped with a field-effect transistor (FET) and feedback network for initial amplification, both housed within the vacuum capsule at the detector liquid nitrogen temperature. The FET output is sent to a preamplifier located outside the vacuum, which provides two outputs, one of which is directed to the digitizer (CAEN DT5780) for energy measurement.

3. Signal Processing and Trapezoidal Filtering

Both detectors signals, after amplification, are sent to a CAEN digitizer, which calculates the energy of the detected radiation based on the amplitude of the signals. Since the calibration source has a relatively high activity, a trapezoidal filter is employed to prevent pile-up effects, ensuring accurate energy readings by smoothing the signals.

The trapezoidal filter is characterized by three key parameters - decay time, rise time, and flat top duration - that need to be optimized to improve the energy resolution of the detectors. Note that the parameters were evaluated, looking at the second ^{22}Na peak at 1275 keV , by taking into account different values of the energy gain for the two detector: 5 for the NaI(Tl) and 1 for HPGe. The final filter parameters for both the NaI(Tl) and HPGe detectors are listed in Table 1:

| Detector | Decay Time [ns] | Rise Time [ns] | Flat Top [ns] | FWHM at 1275 keV [ADC channels] | R |
|----------|-----------------|----------------|---------------|---------------------------------|-------|
| NaI(Tl) | 300 | 400 | 100 | 111 ± 1 | 3.13% |
| HPGe | 52000 | 2000 | 1000 | 5.55 ± 0.06 | 0.19% |

Table 1. Optimized trapezoidal filter parameters for both detectors.

The threshold values for the detectors have been set at the beginning of the data taking, paying attention to the fact that the emission of ^{241}Am has an energy of $E_{\text{peak}}(^{241}\text{Am}) \sim 59\text{ keV}$. The values are shown in Equation 1

$$\text{Threshold}_{\text{NaI(Tl)}} = 20\text{ lsb} \qquad \text{Threshold}_{\text{HPGe}} = 80\text{ lsb} \qquad (1)$$

4. Detectors calibration

In this experiment, energy and efficiency calibrations were performed for the two gamma-ray detectors: NaI(Tl) scintillator and HPGe detector.

Energy calibration. Energy calibration is essential to establish a relationship between the energy of detected gamma rays and the analog-to-digital converter (ADC) counts in the acquired spectra. The calibration function for both detectors is expressed as:

$$E_{\text{peaks}}[\text{keV}] = \alpha_k E_{\text{known}}[\text{ADC}] + \beta_k \qquad \text{where} \qquad k = 0, 1 \quad \text{depending on the channel} \qquad (2)$$

For the energy calibration we used as reference the gamma-ray emissions from known radioactive sources, precisely ^{22}Na and ^{241}Am . Their decays are reported below in Equations 3 and 4. Measurements were conducted over 10 minutes with the shielded well closed and the energy peaks identified in the spectra corresponding to the 59.5 keV (Am-241), 511 keV and 1274.5 keV (Na-22) gamma lines.

$$^{241}\text{Am} \xrightarrow{\alpha} ^{237}\text{Np}^* \quad \text{b.r. 85\%} \quad \xrightarrow[\text{Transition}]{\text{Energy}} \quad \Delta E(^{237}\text{Np}^*) = 59.54 \text{ keV} \quad (3)$$

$$^{22}\text{Na} \xrightarrow{\beta^+} ^{22}\text{Ne}^* + e^+ + \nu_e \quad \text{b.r. 90\%} \quad \xrightarrow[\text{Transition}]{\text{Energy}} \quad \Delta E(e^+e^-) = 511 \text{ keV} \quad \text{and} \quad \Delta E(^{22}\text{Ne}^*) = 1274.54 \text{ keV} \quad (4)$$

For each spectrum of each detector, the background from a 15-minute acquisition is subtracted. Then, a Gaussian fit is performed within the region of interest of the peaks to determine the value of $E_{\text{known}}(\text{ADC})$, defined as the mean of the Gaussian fit.

Efficiency calibration. The efficiency calibration of gamma-ray detectors is a crucial step to quantify their ability to detect photons of specific energies. This calibration aims to establish a relationship between the number of photons detected under a photo-peak and the actual number of photons emitted by a radioactive source. To achieve this, an important parameter is the intrinsic efficiency of a detector, which is defined as the ratio between the number of detected photons at a given energy and the number of photons of that energy that hit the detector:

$$\varepsilon_{\text{intrinsic}} = \frac{N_{\text{detected}}(E)}{\Delta t \cdot A \cdot \text{BR} \cdot \varepsilon_g} \quad (5)$$

- $N_{\text{detected}}(E)$ is the net count under the photo-peak of energy E ;
- Δt is the acquisition time;
- A is the source activity;
- BR is the branching ratio of the decay transition;
- $\varepsilon_g = \frac{\pi r^2}{4\pi d^2}$ is the geometric efficiency that accounts for the fraction of the solid angle covered by the detector, where r is the detector radius and d is the source-detector distance.

Operationally the efficiency calibration is achieved as follows: at first it is necessary to collect the spectra acquisition at given distances from the sources, whose activity is known. Once the spectra are obtained, the background subtraction is carried out in order to isolate the source signal from the background noise. For the emerging peaks of interest, we compute the value of N_{detected} by executing a gaussian fit and integrating 2σ around the energy mean. Moreover, by measuring the respective distances of the sources from the detectors, the geometric efficiency ε_g is evaluated. At this point, the different values of $\varepsilon_{\text{intrinsic}}$ related to the same detector are plotted and fitted through the exponential function in Equation 6, which provides a relation between the intrinsic efficiency and the energy.

$$\epsilon = Ae^{(E/\tau)} + f \quad (6)$$

4.1 NaI(Tl) calibration

Energy calibration. The results of the the energy calibration fit for the NaI(Tl) detector are presented in Figure 1 and Table 2.

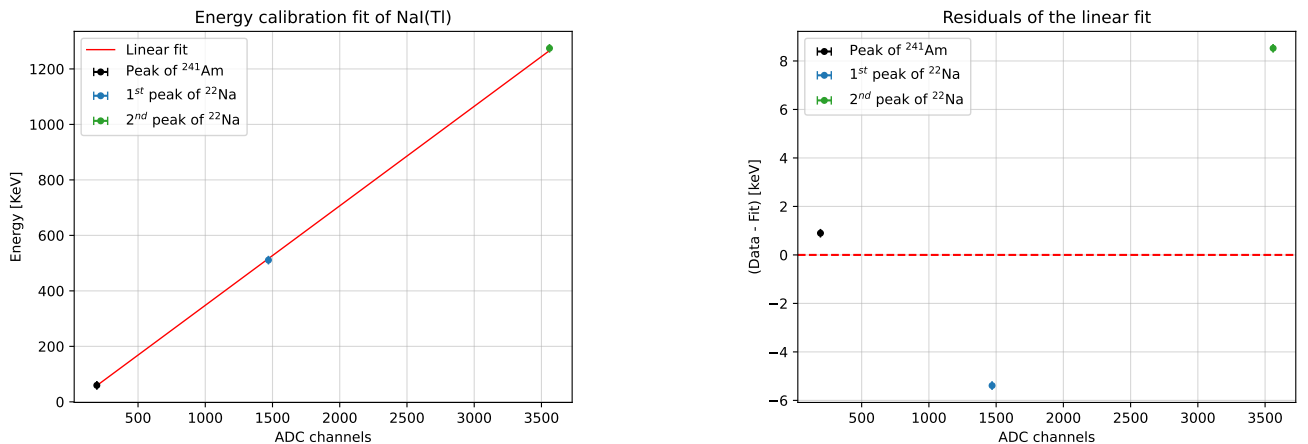


Figure 1. Calibration fit of the NaI(Tl) detector and its residuals.

| α [keV/ADC] | β [keV] | χ^2 |
|-----------------------|-------------------|----------|
| 0.35867 ± 0.00003 | -10.80 ± 0.03 | 12885 |

Table 2. NaI(Tl) energy calibration fit parameters.

Efficiency Calibration. In order to derive the intrinsic efficiency of the NaI(Tl) detector the spectra of ^{22}Na , ^{60}Co and ^{241}Am were collected for about 10 minutes with the shielded well closed. To exploit the calibration fit we considered the first and second peak of both ^{22}Na and ^{60}Co as well as the peak of ^{241}Am , as shown in Figure 2. The sources were placed respectively at $d_{\text{Na-22}} = (8.15 \pm 0.05)$ cm, $d_{\text{Co-60}} = (7.30 \pm 0.05)$ cm and $d_{\text{Am-241}} = (7.20 \pm 0.05)$ cm from the NaI(Tl). The parameters obtained from the calibration fit are shown in Table 3.

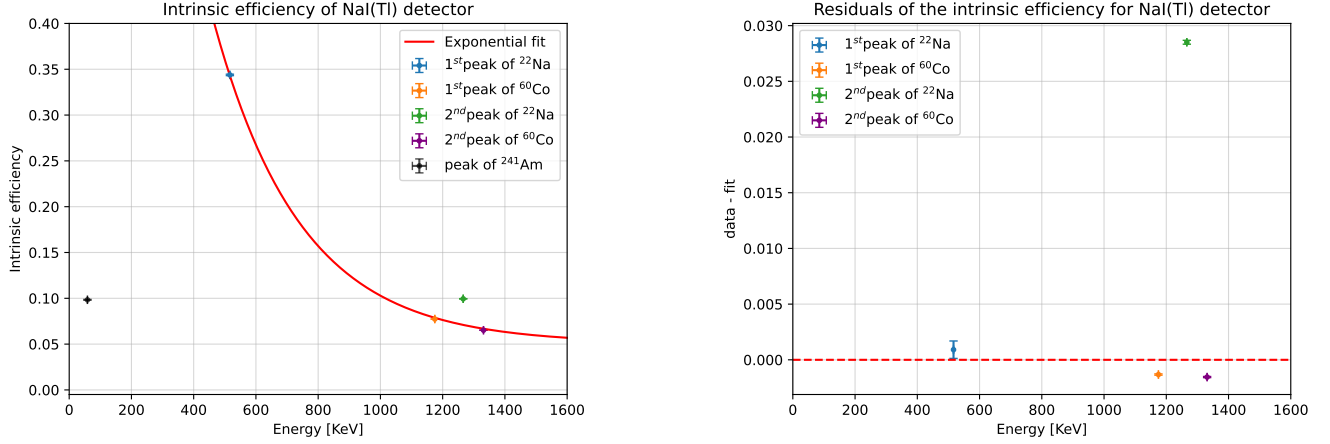


Figure 2. NaI(Tl) intrinsic efficiency fit and its residuals

| A | τ [keV] | f |
|-----------------|--------------|-------------------|
| 1.84 ± 0.02 | -281 ± 1 | 0.005 ± 0.002 |

Table 3. NaI(Tl) intrinsic efficiency fit parameters.

4.2 HPGe calibration

Energy Calibration. The results of the the energy calibration fit for the HPGe detector are presented in Figure 3 and Table 4.

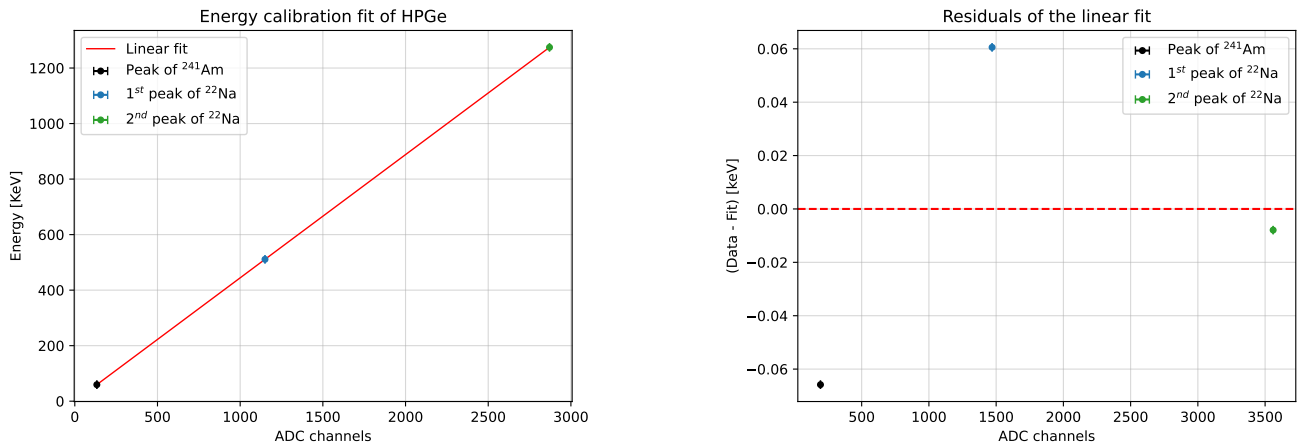


Figure 3. Calibration fit of the HPGe detector and its residuals

| α [keV/ADC] | β [keV] | χ^2 |
|-----------------------|-----------------|----------|
| 0.44384 ± 0.00002 | 0.47 ± 0.05 | 2.78 |

Table 4. Energy calibration fit parameters.

Efficiency Calibration. In the case of the HPGe detector, the efficiency calibration is carried out studying the spectrum of ^{152}Eu . Data acquisition for the ^{152}Eu source, placed at $d_{\text{Eu-152}} = (20.00 \pm 0.05)$ cm from the HPGe, was performed for approximately 20 minutes with the shielded well closed. This source provides multiple well-defined gamma-ray lines due to its beta decay modes covering a wide range of energy values as highlighted in Figure 4 below, while the correspondent branching ratios are presented in Table 5. The efficiencies, calculated as explained in Equation 5, are shown in Figure 5; the resulting fit parameters are in Table 6.

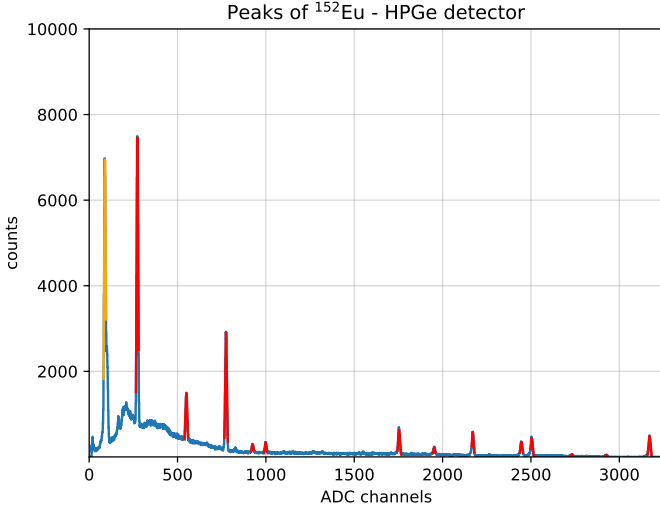


Figure 4. Peaks of ^{152}Eu . The orange peak consists of an X-ray emission, given by electronic rearrangement.

| Energy [keV] | BR | $\varepsilon_{\text{intrinsic}}$ |
|------------------|-----------------------|----------------------------------|
| 121.7 ± 0.2 | 0.284 ± 0.001 | 1.363 ± 0.008 |
| 244.7 ± 0.2 | 0.0755 ± 0.0004 | 1.33 ± 0.01 |
| 344.3 ± 0.2 | 0.266 ± 0.001 | 0.570 ± 0.004 |
| 411.1 ± 0.2 | 0.02238 ± 0.0001 | 1.01 ± 0.02 |
| 444.0 ± 0.2 | 0.028 ± 0.0002 | 0.81 ± 0.01 |
| 778.9 ± 0.2 | 0.1297 ± 0.0006 | 0.293 ± 0.004 |
| 867.2 ± 0.2 | 0.0424 ± 0.0002 | 0.366 ± 0.007 |
| 964.1 ± 0.2 | 0.145 ± 0.0006 | 0.224 ± 0.003 |
| 1086.2 ± 0.2 | 0.1013 ± 0.0006 | 0.235 ± 0.004 |
| 1112.1 ± 0.2 | 0.1341 ± 0.0006 | 0.196 ± 0.003 |
| 1213.1 ± 0.3 | 0.01416 ± 0.00009 | 0.31 ± 0.01 |
| 1299.5 ± 0.2 | 0.01633 ± 0.00009 | 0.190 ± 0.007 |
| 1408.1 ± 0.2 | 0.2085 ± 0.0008 | 0.137 ± 0.002 |

Table 5. Branching ratios taken from the LNHBB website and values of the intrinsic efficiencies.

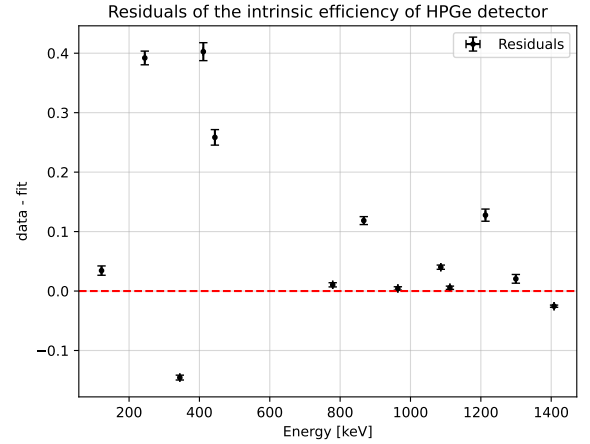
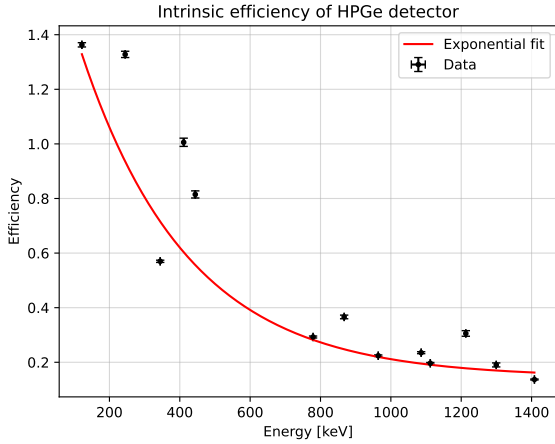


Figure 5. HPGe intrinsic efficiency fit and its residuals

| A | τ [keV] | f |
|-----------------|--------------|-------------------|
| 1.76 ± 0.02 | -305 ± 4 | 0.145 ± 0.002 |

Table 6. HPGe intrinsic efficiency fit parameters.

| A | τ [keV] | f |
|-----------------|--------------|-------------------|
| 1.77 ± 0.01 | -401 ± 5 | 0.087 ± 0.003 |

Table 7. Corrected HPGe intrinsic efficiency fit parameters.

Data number two and three report χ^2 values respectively of $\chi^2_2 = 1159.82$ and $\chi^2_3 = 1268.47$. Therefore the intrinsic efficiency calibration was performed neglecting these data, leading to the fit displayed in Figure 6. The resulting parameters of the new calibration fit are shown in Table 7.

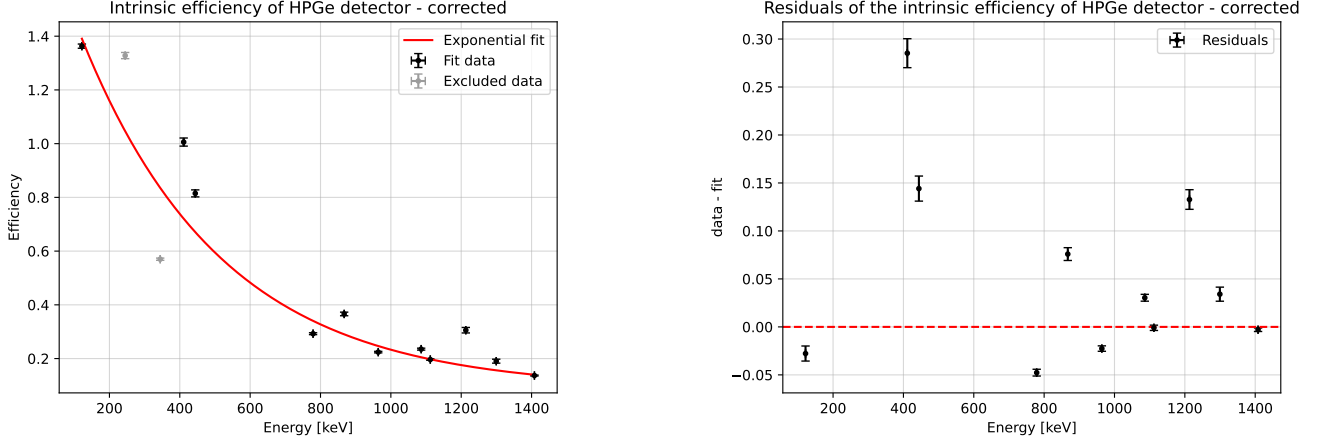


Figure 6. Corrected HPGe intrinsic efficiency fit and its residuals

Relative Efficiency Calibration. Re-normalizing to 1 the intrinsic efficiency value associated to the 1408 keV peak and coherently all the others intrinsic efficiency values, it's possible to calculate the relative values of peak efficiencies as explained in Equation 7 and therefore, plotting these new values, implementing the relative efficiency calibration.

$$\varepsilon_{\text{relative}}(E) = \frac{N(E) \cdot I(1408\text{KeV})}{N(1408\text{KeV}) \cdot I(E)} \quad (7)$$

where N is the number of detected photons and I is the relative intensity. The values of the relative intensities for the detected peaks are reported in Table 8.

The results are shown in Figure 7 and in Table 9.

| Energy [keV] | Intensity [%] | $\varepsilon_{\text{relative}}$ |
|------------------|-----------------|---------------------------------|
| 121.7 ± 0.2 | 141.0 ± 4.0 | 9.6 ± 0.3 |
| 244.7 ± 0.2 | 37.0 ± 1.0 | 9.6 ± 0.3 |
| 344.3 ± 0.2 | 127.0 ± 1.0 | 4.2 ± 0.1 |
| 411.1 ± 0.2 | 10.4 ± 0.1 | 7.4 ± 0.2 |
| 444.0 ± 0.2 | 15.0 ± 0.2 | 5.3 ± 0.1 |
| 778.9 ± 0.2 | 62.6 ± 0.6 | 2.1 ± 0.2 |
| 867.2 ± 0.2 | 20.5 ± 0.2 | 2.65 ± 0.07 |
| 964.1 ± 0.2 | 70.4 ± 0.7 | 1.62 ± 0.04 |
| 1086.2 ± 0.2 | 48.7 ± 0.5 | 1.71 ± 0.04 |
| 1112.1 ± 0.2 | 65.0 ± 0.7 | 1.42 ± 0.03 |
| 1213.1 ± 0.3 | 6.7 ± 0.1 | 2.27 ± 0.09 |
| 1299.5 ± 0.2 | 7.8 ± 0.1 | 1.40 ± 0.06 |
| 1408.1 ± 0.2 | 100.0 ± 1.0 | 1 ± 0.02 |

Table 8. Relative intensities of the detected gamma transitions of ^{152}Eu and values of the relative efficiencies.

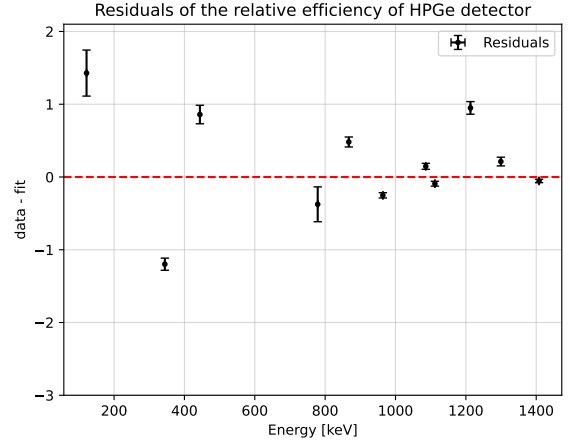
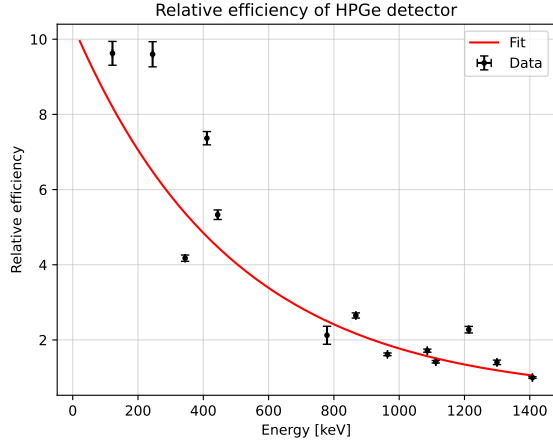


Figure 7. HPGe relative efficiency fit and its residuals

| A | τ [keV] | f |
|---------------|------------------------|-----------------|
| 9.9 ± 0.2 | $(-49 \pm 2) \cdot 10$ | 0.51 ± 0.07 |

Table 9. HPGe relative efficiency fit parameters.

| A | τ [keV] | f |
|----------------|------------------------|-----------------|
| 13.5 ± 0.4 | $(-41 \pm 1) \cdot 10$ | 0.61 ± 0.05 |

Table 10. Corrected HPGe relative efficiency fit parameters.

In this case, differently from the previous case, the third and fourth peaks are the ones that show an anomalous χ^2 value, namely $\chi^2_3 = 206.30$ and $\chi^2_4 = 219.52$. As a result, the fit has been performed neglecting the pathological data data, as shown in Figure 8. The final results are presented in Table 10.

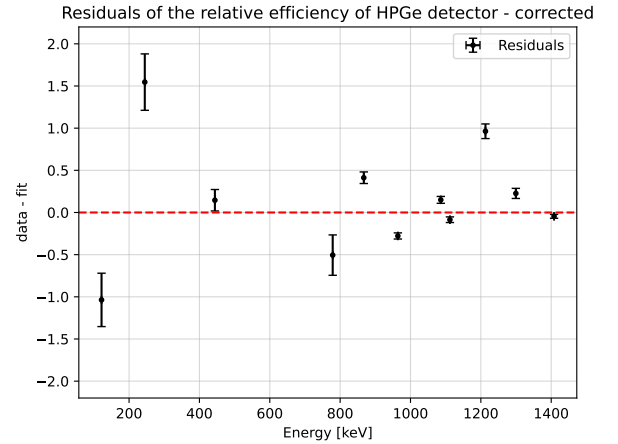
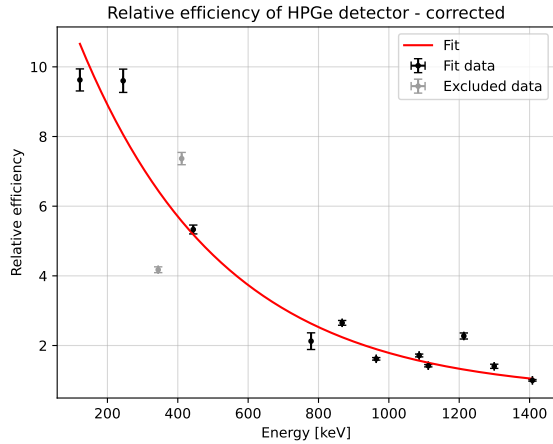


Figure 8. Corrected HPGe relative efficiency fit and its residuals

From the results obtained in this section we can conclude that the HPGe detector exhibits consistent and reasonable peak values, with intrinsic and relative efficiencies following the expected exponential trend. Some computed intrinsic efficiencies greater than 1 may result from inaccuracies in the estimation of source-detector distance and therefore in the solid angle. In contrast, the NaI(Tl) detector shows issues at low energies, particularly for the ^{241}Am source, where the counts emerged to be significantly lower than expected. This discrepancy disrupts the typical exponential trend of the intrinsic efficiency. To address such behavior, we performed an analysis of the acquired data without background correction and we cross-checked the ^{241}Am source activity, but it was unsuccessful: the HPGe detector recorded a reasonable number of counts at low energy, in agreement with expectation. This suggests a configuration issue in the NaI(Tl) detector, likely related to its threshold or energy gain settings, preventing proper acquisition at low energies. Despite these issues, the NaI(Tl) detector's efficiency remains reliable for high-energy emissions, as shown by the consistent data for ^{22}Na and ^{60}Co sources. For low-energy analyses, however, the HPGe detector should be used exclusively due to its superior performance in this range.

5. Samples analysis

In this section, different samples were analyzed using gamma-ray spectroscopy, with the purpose of identifying the presence of radionuclides and of measuring the activity of each source. As we did in the previous sections, the background is subtracted from the sample spectra and the relevant peaks are fitted with a gaussian curve. The activity of the samples, associated to each transition, is computed as follows:

$$A = \frac{N_{\text{peak}}}{m \epsilon \Delta t \epsilon_g \text{BR}(\gamma)} \quad (8)$$

- N_{peak} is the area under the specific peak, obtained by performing a Gaussian fit in the peak region and integrating¹ accordingly;
- Δt is the acquisition time, which is constant for all the analyzed samples;
- ϵ_g is the geometric efficiency. As in the previous sections, it is computed using the measured distances of the samples from the detectors;
- m is the mass of each sample, summarized in Table 11;
- ϵ is the peak efficiency at different energies, computed by using the parameters obtained in the previous section;
- $\text{BR}(\gamma)$ is the branching ratio associated to the decay, in particular to the gamma production of interest.

Before analyzing the acquired spectra, it is important to remark that in order to give a reasonable estimate of the activity of each sample, a greater acquisition time was required. In addition, since the samples were positioned at a small distance from the detectors, the uncertainties associated to the geometric efficiencies of both detectors are inevitably large and of difficult evaluation. During the experiment, we placed every sample at a constant distance of $d_{\text{NaI}} = (3.00 \pm 0.05)$ cm from the NaI(Tl) detector and of $d_{\text{HPGe}} = (6.05 \pm 0.05)$ cm from the HPGe detector.² As a result, we estimated the geometric efficiencies of both detectors to be:

$$\epsilon_g^{\text{NaI}} \sim 0.391 \quad \epsilon_g^{\text{HPGe}} \sim 0.026 \quad (9)$$

As a final remark, as it was pointed out in the previous sections, the NaI(Tl) detector did not behave as expected at low energies. Indeed, by looking at the spectra acquired, it is evident that the peaks height (counts) with the NaI(Tl) and HPGe detectors do not share the same trend: the NaI detector registers far less counts in the low-energy region.³

Despite such premise, we analyzed all samples spectra with both detectors and provided, for every detected gamma energy peak, the corresponding possible radionuclide and the expected energy of its gamma emission. The comprehensive list can be found in the appendix.

| Sample | KCl | Mushrooms | Cement | ZrO ₂ | Autunite |
|------------------|-------|-----------|--------|------------------|----------|
| Weight [g] | 162.2 | 18.7 | 500.2 | 1157.2 | 31.8 |
| Δt [min] | 15 | 15 | 15 | 15 | 15 |

Table 11. Acquisition time and weight of the analyzed samples.

Autunite. Autunite is a mineral with a significant uranium content, consisting of approximately 48.27% uranium by weight. This high uranium concentration makes it a naturally radioactive mineral. The uranium primarily exists in the form of ²³⁸U, which undergoes a long decay chain. Due to this, autunite exhibits measurable radioactivity, detectable via gamma-ray spectroscopy. In the gamma spectrum shown in Figure 9, prominent peaks correspond to radionuclides from the decay chain of ²³⁸U, specifically ²²⁶Ra and its progeny: ²¹⁴Pb and ²¹⁴Bi. The corresponding total activities of the expected radionuclides are summarized, for each detector, in Table 12 and Table 13.

¹In this section, for the analysis of all spectra, we computed the Gaussian integrals around 2σ from the mean.

²The distances were measured considering each sample as pointlike, the point being the geometric center of the plastic canister. In doing so, we assumed the geometric center to coincide with the center of mass of the sample.

³As we discussed in the previous sections, this pathological behavior may be due to the chosen settings of the NaI(Tl) detector.

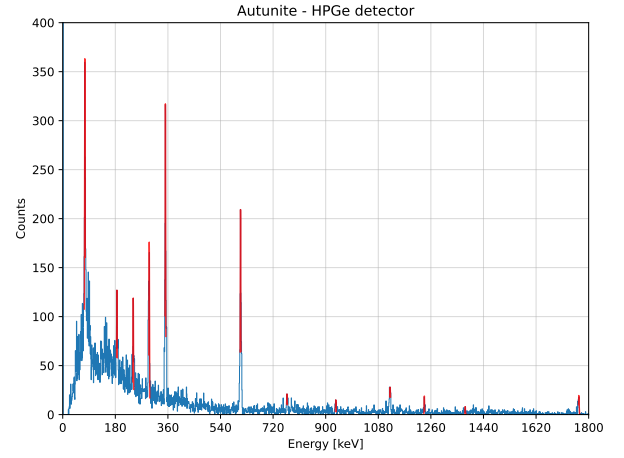
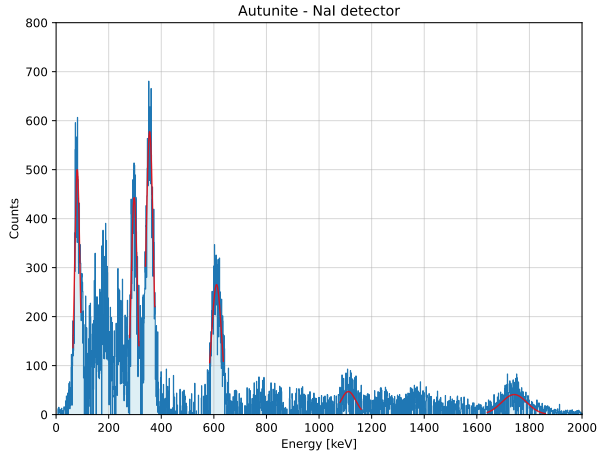


Figure 9. Spectra of the autunite sample: on the left the spectrum acquired with the NaI(Tl) detector, on the right the spectrum acquired with the HPGe detector.

| NaI(Tl) | |
|-------------------|------------------|
| Isotope | Activity [Beq/g] |
| ^{214}Pb | 32.1 ± 0.4 |
| ^{226}Ra | 26.8 ± 0.3 |
| ^{214}Bi | 82 ± 1 |

Table 12. Radionuclides detected in the autunite sample with the NaI(Tl) detector, together with the computed activities.

| HPGe | |
|-------------------|------------------|
| Isotope | Activity [Beq/g] |
| ^{214}Pb | 29 ± 1 |
| ^{226}Ra | 18.7 ± 0.7 |
| ^{214}Bi | 45 ± 5 |

Table 13. Radionuclides detected in the autunite sample with the HPGe detector, together with the computed activities.

Porcini Mushrooms. Fungi, which lack stems and roots, use absorption to obtain nutrition from the atmosphere through their surface cells. As a result, mushrooms are prone to absorb radionuclides present in their surrounding biome. By analyzing their spectrum, we looked for the presence of naturally and artificially occurring radionuclides. As summarized in Table 14 and Table 15, we were able to detect small traces of the artificial radioactive isotope ^{137}Cs , mainly released into the environment after nuclear accidents, indicated by the characteristic 662 keV peak. Such peak was only visible with the NaI(Tl) detector, thanks to its characteristic faster acquisition rate. As a remark, it is important to notice the fairly low statistics of the acquired data, which not only made the analysis harder but undermined the accuracy of the estimations.

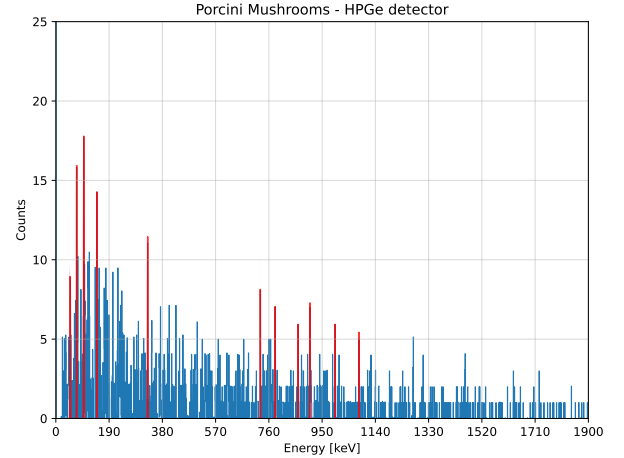
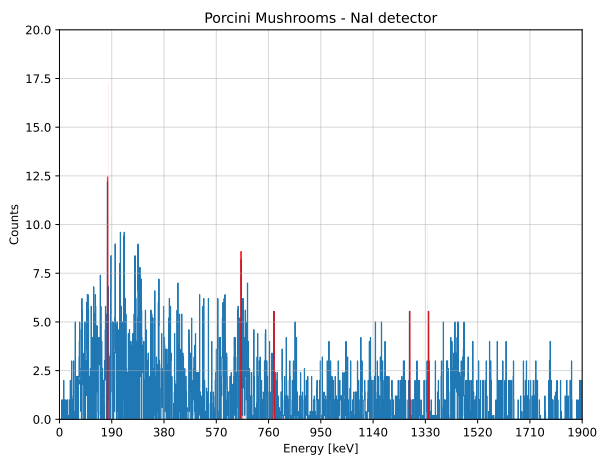


Figure 10. Spectra of the porcini mushrooms' sample: on the left the spectrum acquired with the NaI(Tl) detector, on the right the spectrum acquired with the HPGe detector.

| NaI(Tl) | |
|-------------------|-------------------|
| Isotope | Activity [Beq/g] |
| ^{214}Pb | 1.1 ± 0.3 |
| ^{226}Ra | 0.08 ± 0.02 |
| ^{137}Cs | 0.012 ± 0.002 |
| ^{40}K | 0.17 ± 0.04 |

Table 14. Radionuclides detected in the sample of porcini mushrooms with the NaI(Tl) detector, together with the computed activities.

| HPGe | |
|-------------------|------------------|
| Isotope | Activity [Beq/g] |
| ^{214}Pb | 7 ± 2 |
| ^{212}Bi | 31 ± 7 |
| ^{234}Pa | 29 ± 8 |
| ^{212}Pb | 0.31 ± 0.06 |
| ^{208}Tl | 0.5 ± 0.1 |

Table 15. Radionuclides detected in the sample of porcini mushrooms with the HPGe detector, together with the computed activities.

Potassium Chloride. Potassium chloride KCl is a metal halide salt composed of potassium and chlorine. A sample of KCl was analyzed to determine the activity of ^{40}K , a natural isotope of potassium with an isotopic abundance of 0.0117 (1)%. It disintegrates by β^- decay to the ^{40}Ca fundamental level for 89.25%, and by electron capture to an excited state of ^{40}Ar for 10.55%. In the latter decay path, ^{40}K emits a 1460.82 keV gamma-ray which can be easily seen in the spectrum acquired by both detectors, presented in Figure 11.⁴ The estimated activity of the detected ^{40}K , for both NaI(Tl) and HPGe detectors, is presented below

$$A_{^{40}\text{K}}^{\text{NaI}} = 23.4 \pm 0.3 \text{ [Beq/g]} \quad A_{^{40}\text{K}}^{\text{HPGe}} = 6.8 \pm 0.4 \text{ [Beq/g]} \quad (10)$$

The non compatibility of the two activities above is a clear index of the different operating specifics of the NaI(Tl) and HPGe detectors, which differ not only in resolution and efficiency, but also in acquisition rate.

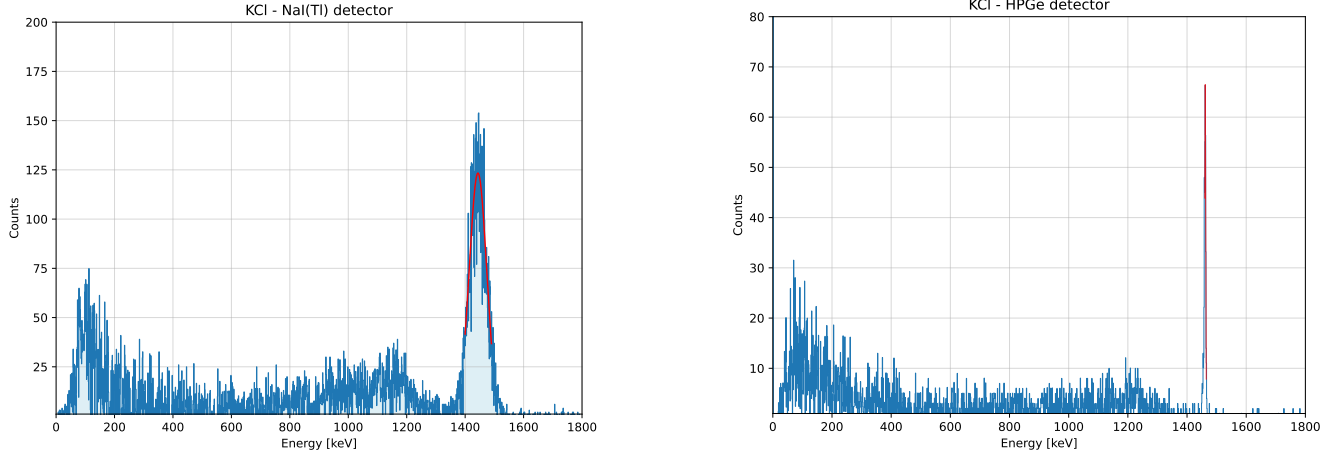


Figure 11. Spectra of the Potassium Chloride sample: on the left the spectrum acquired with the NaI(Tl) detector, on the right the spectrum acquired with the HPGe detector.

Zirconium Dioxide. Zirconium Dioxide ZrO_2 , sometimes known as zirconia, is a white crystalline oxide of zirconium. Typically contains trace amounts of radionuclides such as radium, thorium, and uranium. Products of the ^{232}Th chain are found, such as ^{208}Tl and ^{228}Ac , together with others that come from the radioactive series of ^{226}Ra , i.e. ^{214}Pb and ^{214}Bi . The corresponding activities are calculated and reported in Table 16 and Table 17, whereas the acquired spectra are shown in Figure 12. The gamma spectrum of a radium source exhibits many lines but the peak at 186 keV is the only one that comes directly from the ^{226}Ra decay, namely from an excited state of ^{222}Rn .

⁴Indeed, it is the only gamma decay that can be truthfully deduced by the spectra we acquired, as all the other peaks are, in comparison, not statistically relevant.

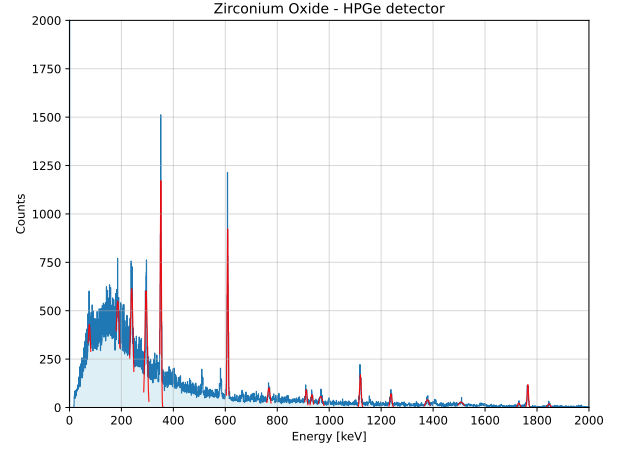
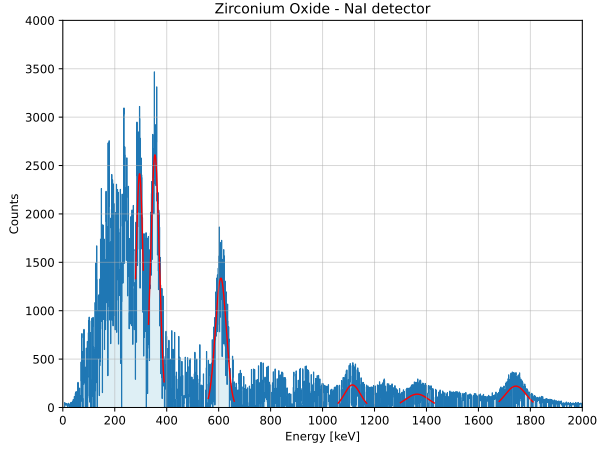


Figure 12. Spectra of the Zirconium Dioxide sample: on the left the spectrum acquired with the NaI(Tl) detector, on the right the spectrum acquired with the HPGe detector.

| NaI(Tl) | |
|-------------------|------------------|
| Isotope | Activity [Beq/g] |
| ^{214}Pb | 3.10 ± 0.03 |
| ^{214}Bi | 27.6 ± 0.2 |

Table 16. Radionuclides detected in the sample of zirconium dioxide with the NaI(Tl) detector, together with the computed activities.

| HPGe | |
|-------------------|------------------|
| Isotope | Activity [Beq/g] |
| ^{214}Pb | 8.7 ± 0.1 |
| ^{228}Ac | 9.6 ± 0.2 |
| ^{226}Ra | 11.1 ± 0.1 |
| ^{208}Tl | 0.58 ± 0.02 |
| ^{214}Bi | 12.9 ± 0.6 |

Table 17. Radionuclides detected in the sample zirconium dioxide with the HPGe detector, together with the computed activities.

Portland Cement. Portland cement is the most common type of cement in general use around the world as a basic ingredient of concrete, mortar, stucco, and non-specialty grout. Since Portland cement is derived from natural materials such as limestone and clay, it often contains trace amounts of naturally occurring radionuclides. These radionuclides originate primarily from the decay chains of ^{238}U (leading to ^{214}Pb , ^{214}Bi), ^{232}Th (leading to ^{212}Pb) and ^{40}K . While the presence of ^{40}K is expected, given its prevalence in silicate minerals, the presence of ^{22}Na is less common and may indicate trace contamination. We present the acquired spectra in Figure 13, while in Table 18 and Table 19 we summarize the total activity of the detected radionuclides.

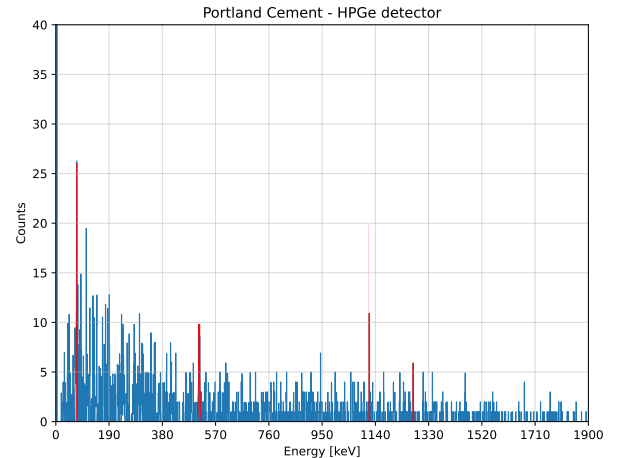
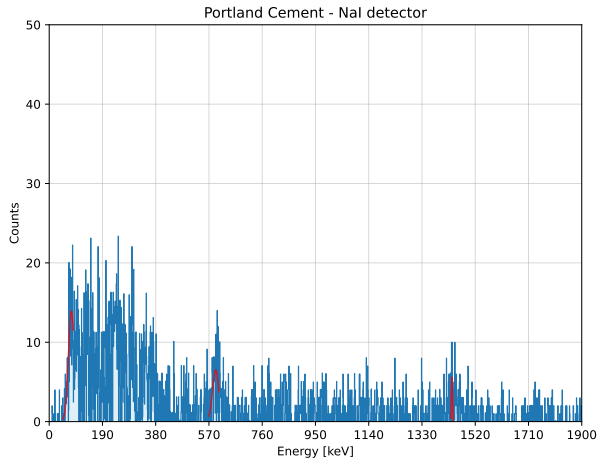


Figure 13. Spectra of the Portland cement sample: on the left the spectrum acquired with the NaI(Tl) detector, on the right the spectrum acquired with the HPGe detector.

| NaI(Tl) | |
|-------------------|---------------------|
| Isotope | Activity [Beq/g] |
| ^{214}Pb | 0.0157 ± 0.0008 |
| ^{214}Bi | 0.0038 ± 0.0002 |
| ^{40}K | 0.010 ± 0.002 |

Table 18. Radionuclides detected in the sample of Portland cement with the NaI(Tl) detector, together with the computed activities.

| HPGe | |
|-------------------|---------------------|
| Isotope | Activity [Beq/g] |
| ^{22}Na | 0.005 ± 0.001 |
| ^{212}Pb | 0.025 ± 0.003 |
| ^{214}Bi | 0.0127 ± 0.0004 |

Table 19. Radionuclides detected in the sample of Portland cement with the HPGe detector, together with the computed activities.

6. Radon counting

In order to measure the activity of ^{222}Rn in an indoor environment, a canister with activated charcoal was initially weighed finding a mass of $m_i = (151.90 \pm 0.03)\text{g}$. It was later opened, exposed for 50 hours, closed and weighed again with a result of $m_f = (157.50 \pm 0.03)\text{g}$. The increase of weight is due to an absorption of water. A mass variation of $\Delta m_{50h} = (5.60 \pm 0.04)\text{g}$, resulting from a 50 hours exposure, can be normalized as a mass variation of $\Delta m_{48h} = (5.38 \pm 0.04)\text{g}$ resulting from a 48 hours exposure. Such mass gain corresponds to a percentage of humidity of 80%. From this reference value of humidity we can extrapolate the relative values of CF(48h), AF(48h), which are respectively the calibration factor and the adjustment factor for a 2-day exposure and AF(50h) which is the adjustment factor for a $T_s = 50\text{h}$ exposure according to EPA standards. The values are shown in Equation 11.

$$CF = CF(48h) \times \frac{AF(T_s)}{AF(48h)} \sim 0.097\text{L/min} \quad \text{using} \quad \begin{aligned} CF(48h) &= 0.097\text{L/min} \\ AF(48h) &= 0.093\text{L/min} \\ AF(50h) &= 0.090\text{L/min} \end{aligned} \quad (11)$$

Finally the radon activity can be estimated from Equation 12, whose parameters are defined below:

$$RN = \frac{N}{(DF \times E \times CF \times T_s)} \quad (12)$$

- N is the net number of counts obtained from the exposed canister;
- DF is a decay factor which takes into consideration the part of Radium in the canister which may decay before being detected;
- E is the net number of counts obtained from the calibrated canister normalised to the activity of the source;⁵
- CF is the calibration factor already explained;
- T_s is time exposure of the canister;

In particular DF is calculated as explained in Equation 13

$$DF = e^{-\frac{\ln(2) \cdot t}{T_{1/2}}} \sim 0.828 \quad (13)$$

where t is half of the time of the exposure and $T_{1/2}$ is the Radium decay time taken from the LNHB website. The values of N and E have been calculated respectively from the exposed canister and from the calibrated one after subtracting the background of an unexposed canister and calibrating the data with the coefficients of Section 4. The spectra for the calibrated canister and for the exposed one can be found in Figure 14 and 15 respectively. The values of N and E are reported in Table 20 below.

⁵Source number 105 of the Polo Didattico with an activity of $A = 0.370\text{ kBq}$ on 27/01/1992. The nowadays activity has been evaluated from the $T_{1/2}^{226\text{Ra}}$ taken from the LNHB website.

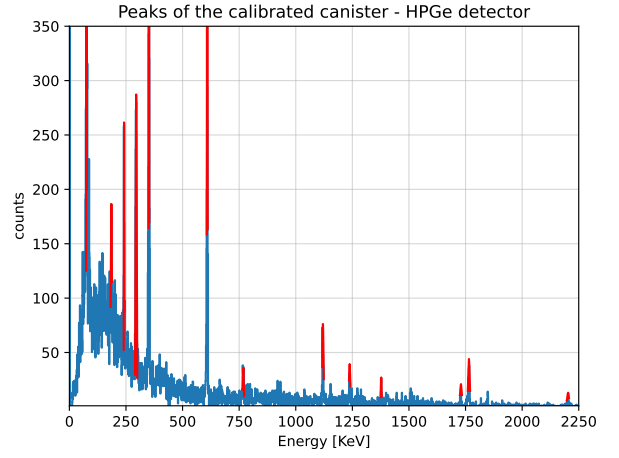
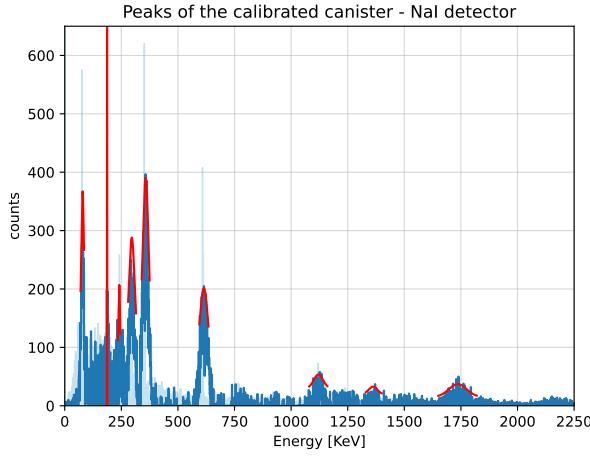


Figure 14. Spectra of the calibrated canister: on the left the spectrum acquired with the NaI(Tl) detector, on the right the spectrum acquired with the HPGe detector.

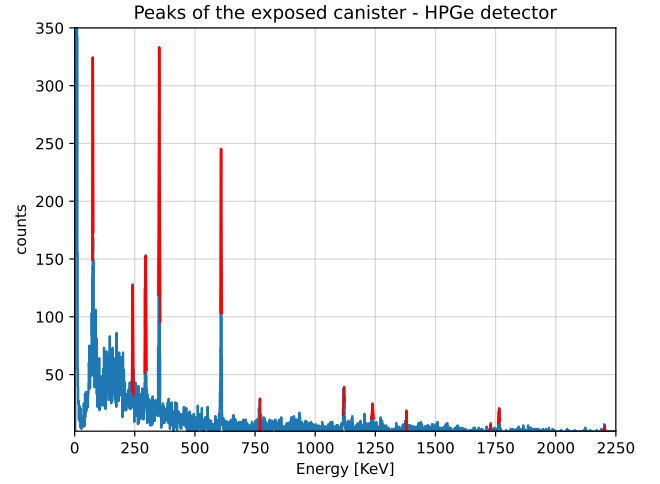
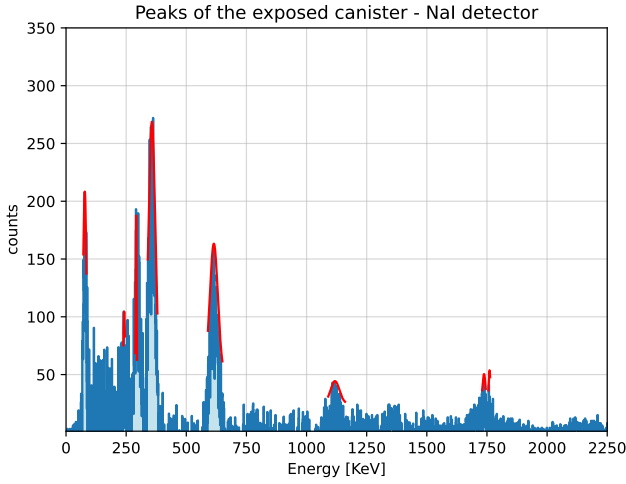


Figure 15. Spectra of the exposed canister: on the left the spectrum acquired with the NaI(Tl) detector, on the right the spectrum acquired with the HPGe detector.

| detector | N | E |
|----------|---------------------------------|----------------------------|
| NaI(Tl) | $(174 \pm 1) \cdot 10^2$ counts | (81.9 ± 0.5) counts/Bq |
| HPGe | $(521 \pm 7) \cdot 10$ counts | (23.4 ± 0.2) counts/Bq |

Table 20. Values of N and E for both the detectors

From these we found

$$RN_{\text{NaI(Tl)}} = (879 \pm 8) \text{ Bq/m}^3 \quad RN_{\text{HPGe}} = (921 \pm 16) \text{ Bq/m}^3 \quad (14)$$

It is evident that both of these values exceed a lot the European limit of Radon concentration for indoor environment, which is of 300 Bq/m^3 . The overestimation of the radon concentration we observed is likely due to the water gain being significantly lower than others under the same humidity conditions (80%), suggesting that the actual humidity was probably lower. However a more accurate esteem of the Radon activity could be done by plotting the number of counts of the exposed canister as a function of the number of counts of the calibrated canister normalised to its activity, and then by performing a linear regression of these data.

7. Conclusions

In this report we performed an analysis of the gamma emission spectra for different samples, both of organic and inorganic origin. It was achieved thanks to two different detectors (NaI(Tl) and HPGe detectors) which were firstly calibrated both in energy and efficiency as explained in Section 4.

The spectra analysis of the samples highlighted the presence of many different radionuclides, discussed in Section 5 and summarized in Table 22. The total activity of each sample, normalized to its measured mass, is provided in Table 21 aside.

A notable discrepancy was observed between activity esteems obtained using the NaI(Tl) and HPGe detectors. This discrepancy, highlighted in Section 5, is attributed to the intrinsic differences between the detectors, including resolution, efficiency, and acquisition rate. Additionally, as noted in Section 4, the NaI(Tl) detector exhibited pathological behavior at low energies, registering significantly fewer counts in this region.

| Sample | Detector | Total activity [Bq/g] |
|------------------|----------|-----------------------|
| Autunite | NaI(Tl) | 141 ± 2 |
| Autunite | HPGe | 93 ± 7 |
| Mushrooms | NaI(Tl) | 1.4 ± 0.3 |
| Mushrooms | HPGe | 70 ± 20 |
| KCl | NaI(Tl) | 23.4 ± 0.3 |
| KCl | HPGe | 6.8 ± 0.4 |
| ZrO ₂ | NaI(Tl) | 30.7 ± 0.3 |
| ZrO ₂ | HPGe | 43 ± 1 |
| Cement | NaI(Tl) | 0.030 ± 0.003 |
| Cement | HPGe | 0.043 ± 0.005 |

Table 21. Total activities of the analysed samples.

An additional analysis of the presence of ^{222}Rn was carried out using a canister filled with activated charcoal. The spectrum of the canister was measured after a two-day exposure and subsequently compared to the spectrum of a calibrated canister containing ^{226}Ra with a known activity. The measured radon concentration was found to be significantly above the European safety limit of 300 Bq/m^3 . Specifically, the esteems are the following:

$$\text{RN}_{\text{NaI(Tl)}} = (879 \pm 8) \text{ Bq/m}^3 \quad \text{and} \quad \text{RN}_{\text{HPGe}} = (921 \pm 16) \text{ Bq/m}^3$$

While it has already been noted that both measurements exceed the European limit by a considerable margin, it is important to highlight that these values are likely overestimated. This overestimation primarily stems from incorrect assumptions regarding the environmental humidity, which significantly impacts the measurement accuracy.

| Detector | Sample | Isotope | BR(γ) [%] | Expected Energy [keV] | Experimental Energy [keV] | N _{peak} | Activity [Beq/g] |
|----------|-----------|-------------------|--------------------|-----------------------|---------------------------|-------------------|---------------------|
| NaI(Tl) | KCl | ⁴⁰ K | 10.55 | 1460.82 | 1444 \pm 2 | 8640 \pm 90 | 23.4 \pm 0.3 |
| HPGe | KCl | ⁴⁰ K | 10.55 | 1460.82 | 1460.9 \pm 0.2 | 360 \pm 20 | 6.8 \pm 0.4 |
| NaI(Tl) | Autunite | ²¹⁴ Pb | 10.47 | 77.1088 | 80.5 \pm 0.7 | 13000 \pm 100 | 7.8 \pm 0.1 |
| NaI(Tl) | Autunite | ²²⁶ Ra | 3.55 | 186.211 | 184 \pm 5 | 10700 \pm 100 | 26.8 \pm 0.3 |
| NaI(Tl) | Autunite | ²¹⁴ Pb | 7.268 | 241.997 | 239 \pm 1 | 4680 \pm 70 | 6.9 \pm 0.1 |
| NaI(Tl) | Autunite | ²¹⁴ Pb | 18.414 | 295.224 | 297.1 \pm 0.8 | 12800 \pm 100 | 9.0 \pm 0.1 |
| NaI(Tl) | Autunite | ²¹⁴ Pb | 35.6 | 351.932 | 355.7 \pm 0.6 | 19200 \pm 100 | 8.5 \pm 0.1 |
| NaI(Tl) | Autunite | ²¹⁴ Bi | 45.49 | 609.312 | 610 \pm 1 | 12000 \pm 100 | 9.1 \pm 0.1 |
| NaI(Tl) | Autunite | ²¹⁴ Bi | 14.91 | 1120.287 | 1111 \pm 4 | 3170 \pm 60 | 22.2 \pm 0.5 |
| NaI(Tl) | Autunite | ²¹⁴ Bi | 15.31 | 1764.494 | 1741 \pm 3 | 4720 \pm 70 | 50.6 \pm 0.8 |
| HPGe | Autunite | ²¹⁴ Pb | 10.47 | 77.1088 | 75.6 \pm 0.5 | 1520 \pm 40 | 12.6 \pm 0.3 |
| HPGe | Autunite | ²²⁶ Ra | 3.55 | 186.211 | 185.6 \pm 0.4 | 590 \pm 20 | 18.7 \pm 0.7 |
| HPGe | Autunite | ²¹⁴ Pb | 7.268 | 241.997 | 241.6 \pm 0.7 | 450 \pm 20 | 7.9 \pm 0.4 |
| HPGe | Autunite | ²¹⁴ Pb | 18.414 | 295.224 | 296.2 \pm 0.2 | 480 \pm 20 | 3.8 \pm 0.2 |
| HPGe | Autunite | ²¹⁴ Pb | 35.6 | 351.932 | 351.50 \pm 0.3 | 930 \pm 30 | 4.3 \pm 0.1 |
| HPGe | Autunite | ²¹⁴ Bi | 45.49 | 609.312 | 608.7 \pm 0.5 | 760 \pm 30 | 4.7 \pm 0.2 |
| HPGe | Autunite | ²¹⁴ Bi | 4.892 | 768.356 | 767.40 \pm 0.3 | 97 \pm 9 | 7.7 \pm 0.7 |
| HPGe | Autunite | ²¹⁴ Bi | 3.1 | 934.34 | 934 \pm 1 | 71 \pm 8 | 11.9 \pm 1.4 |
| HPGe | Autunite | ²¹⁴ Bi | 14.91 | 1120.287 | 1120.3 \pm 0.4 | 170 \pm 10 | 7.9 \pm 0.5 |
| HPGe | Autunite | ²¹⁴ Bi | 5.831 | 1238.111 | 1237.9 \pm 0.3 | 40 \pm 6 | 5.5 \pm 0.8 |
| HPGe | Autunite | ²¹⁴ Bi | 3.968 | 1377.669 | 1377.7 \pm 0.2 | 14 \pm 3 | 3.3 \pm 0.7 |
| HPGe | Autunite | ²¹⁴ Bi | 15.31 | 1764.494 | 1766.107 \pm 0.003 | 56 \pm 7 | 4.5 \pm 0.6 |
| NaI(Tl) | Mushrooms | ²²⁶ Ra | 3.555 | 186.211 | 174.8 \pm 0.7 | 19 \pm 4 | 0.08 \pm 0.02 |
| NaI(Tl) | Mushrooms | ¹³⁷ Cs | 85.01 | 661.657 | 660.3 \pm 0.2 | 15 \pm 3 | 0.012 \pm 0.002 |
| NaI(Tl) | Mushrooms | ²¹⁴ Pb | 1.064 | 785.96 | 779.3 \pm 0.2 | 13 \pm 3 | 1.1 \pm 0.3 |
| NaI(Tl) | Mushrooms | ⁴⁰ K | 10.55 | 1460.822 | 1341 \pm 4 | 8 \pm 2 | 0.17 \pm 0.04 |
| HPGe | Mushrooms | ²¹⁴ Pb | 1.06 | 53.2275 | 51.4 \pm 0.2 | 16 \pm 4 | 2.1 \pm 0.5 |
| HPGe | Mushrooms | ²¹² Pb | 10.07 | 74.8157 | 74.2 \pm 0.6 | 21 \pm 4 | 0.31 \pm 0.06 |
| HPGe | Mushrooms | ²³⁴ Pa | 3.2 | 99.86 | 99.53 \pm 0.01 | 31 \pm 5 | 1.5 \pm 0.2 |
| HPGe | Mushrooms | ²¹² Bi | 0.121 | 328.04 | 327.6 \pm 0.1 | 14 \pm 3 | 31 \pm 7 |
| HPGe | Mushrooms | ²¹² Bi | 6.65 | 727.33 | 729 \pm 15 | 8 \pm 2 | 0.7 \pm 0.2 |
| HPGe | Mushrooms | ²¹⁴ Pb | 1.064 | 785.96 | 782.5 \pm 0.6 | 7 \pm 2 | 4 \pm 1 |
| HPGe | Mushrooms | ²⁰⁸ Tl | 12.4 | 860.53 | 864.2 \pm 0.5 | 8 \pm 2 | 0.5 \pm 0.1 |
| HPGe | Mushrooms | ²³⁴ Pa | 0.34 | 904.2 | 906.6 \pm 0.2 | 11 \pm 3 | 27 \pm 7 |
| NaI(Tl) | Cement | ²¹² Pb | 10.07 | 74.8157 | 79 \pm 2 | 400 \pm 20 | 0.0157 \pm 0.0008 |
| NaI(Tl) | Cement | ²¹⁴ Bi | 45.49 | 609.312 | 594 \pm 3 | 190 \pm 10 | 0.0038 \pm 0.0002 |
| NaI(Tl) | Cement | ⁴⁰ K | 10.55 | 1460.822 | 1437 \pm 1 | 27 \pm 5 | 0.010 \pm 0.002 |
| HPGe | Cement | ²¹² Pb | 10.07 | 74.8157 | 74.5 \pm 0.2 | 46 \pm 6 | 0.025 \pm 0.003 |
| HPGe | Cement | ²² Na | 90.35 * | 511 | 511.4 \pm 0.9 | 33 \pm 5 | 0.0023 \pm 0.0004 |
| HPGe | Cement | ²¹⁴ Bi | 14.91 | 1120.287 | 1118 \pm 11 | 10 \pm 3 | 0.013 \pm 0.004 |
| HPGe | Cement | ²² Na | 99.94 | 1274.537 | 1275 \pm 0.1 | 11 \pm 3 | 0.003 \pm 0.001 |

| Detector | Sample | Isotope | BR(γ) [%] | Expected Energy [keV] | Experimental Energy [keV] | N _{peak} | Activity [Beq/g] |
|----------|------------------|-------------------|--------------------|-----------------------|---------------------------|-------------------|------------------|
| NaI(Tl) | ZrO ₂ | ²¹⁴ Pb | 18.414 | 295.224 | 295 \pm 1 | 92700 \pm 300 | 1.78 \pm 0.02 |
| NaI(Tl) | ZrO ₂ | ²¹⁴ Pb | 35.6 | 351.932 | 354.6 \pm 0.7 | 108500 \pm 300 | 1.31 \pm 0.01 |
| NaI(Tl) | ZrO ₂ | ²¹⁴ Bi | 45.49 | 609.312 | 608 \pm 1 | 66600 \pm 300 | 1.38 \pm 0.02 |
| NaI(Tl) | ZrO ₂ | ²¹⁴ Bi | 14.91 | 1120.287 | 1115 \pm 4 | 17300 \pm 100 | 3.34 \pm 0.03 |
| NaI(Tl) | ZrO ₂ | ²¹⁴ Bi | 3.968 | 1377.669 | 1364 \pm 6 | 17000 \pm 100 | 16.2 \pm 0.1 |
| NaI(Tl) | ZrO ₂ | ²¹⁴ Bi | 15.31 | 1764.494 | 1744 \pm 4 | 22500 \pm 100 | 6.64 \pm 0.04 |
| HPGe | ZrO ₂ | ²¹⁴ Pb | 10.47 | 77.1088 | 76 \pm 1 | 8990 \pm 90 | 2.05 \pm 0.03 |
| HPGe | ZrO ₂ | ²²⁶ Ra | 3.55 | 186.211 | 186 \pm 1 | 12800 \pm 100 | 11.1 \pm 0.1 |
| HPGe | ZrO ₂ | ²¹⁴ Pb | 7.268 | 241.997 | 239.4 \pm 0.4 | 9370 \pm 90 | 4.50 \pm 0.06 |
| HPGe | ZrO ₂ | ²¹⁴ Pb | 18.414 | 295.224 | 295.1 \pm 0.4 | 6480 \pm 80 | 1.39 \pm 0.02 |
| HPGe | ZrO ₂ | ²¹⁴ Pb | 35.6 | 351.932 | 351.7 \pm 0.2 | 6370 \pm 80 | 0.80 \pm 0.01 |
| HPGe | ZrO ₂ | ²²⁸ Ac | 4.45 | 463.002 | 609 \pm 0.3 | 4690 \pm 70 | 8.2 \pm 0.2 |
| HPGe | ZrO ₂ | ²⁰⁸ Tl | 22.5 | 510.74 | 767.8 \pm 0.4 | 1220 \pm 30 | 0.58 \pm 0.02 |
| HPGe | ZrO ₂ | ²²⁸ Ac | 26.2 | 911.196 | 911.2 \pm 0.4 | 830 \pm 30 | 0.44 \pm 0.02 |
| HPGe | ZrO ₂ | ²¹⁴ Bi | 3.1 | 934.34 | 933.3 \pm 0.5 | 710 \pm 30 | 3.3 \pm 0.2 |
| HPGe | ZrO ₂ | ²²⁸ Ac | 15.9 | 968.96 | 967.6 \pm 0.7 | 990 \pm 30 | 0.94 \pm 0.04 |
| HPGe | ZrO ₂ | ²¹⁴ Bi | 14.91 | 1120.287 | 1120 \pm 0.3 | 1210 \pm 30 | 1.54 \pm 0.06 |
| HPGe | ZrO ₂ | ²¹⁴ Bi | 5.831 | 1238.111 | 1237.8 \pm 0.4 | 590 \pm 20 | 2.2 \pm 0.1 |
| HPGe | ZrO ₂ | ²¹⁴ Bi | 3.968 | 1377.669 | 1377.8 \pm 0.8 | 650 \pm 30 | 4.2 \pm 0.2 |
| HPGe | ZrO ₂ | ²¹⁴ Bi | 15.31 | 1764.494 | 1764.4 \pm 0.2 | 730 \pm 30 | 1.62 \pm 0.08 |

Table 22. Summary of prominent gamma energy peaks detected in the spectral analysis of the samples. For each sample, the observed gamma transition energies are listed alongside the corresponding radionuclides, their expected gamma-ray energies, and the number of detected events. Based on these data, the activity [Bq/g] of each identified radionuclide is calculated.